Photochemical & Photobiological Sciences (2023) 22:503–512
https://doi.org/10.1007/s43630-022-00330-z

ORIGINAL PAPERS

Removal of As(III) via adsorption and photocatalytic oxidation with magnetic Fe–Cu nanocomposites

Lucía I. Morán Ayala[1] · Francisca Aparicio[1] · Vittorio Boffa[2] · Giuliana Magnacca[3] · Luciano Carlos[4] · Gabriela N. Bosio[1] · Daniel O. Mártire[1]

Received: 20 August 2022 / Accepted: 20 October 2022 / Published online: 3 November 2022

Abstract

Magnetic Fe–Cu nanocomposites with high adsorption capacity and photocatalytic properties were prepared via the precursor method using soluble substances isolated from urban biowaste (BBS) as carbon sources and different temperatures of the pyrolysis treatment (400, 600, and 800 °C). BBS is used as complexing agent for the Fe^{3+} and Cu^{2+} ions in the precursors. The as-prepared magnetic materials were tested in As(III) removal processes from water. Dark experiments performed with the materials obtained at 400 and 600 °C showed excellent adsorption capacities achieving a significant uptake of 911 and 840 mg g^{-1} for As(III), respectively. Experiments conducted under steady-state irradiation showed a reduction of 50–71% in As(III) levels evidencing the meaningful photocatalytic capacity of Fe–Cu nanocomposites. The best photocatalytic performance was obtained for the nanocomposite synthesized at the highest pyrolysis temperature, in line with the reported trend of $HO^{\cdot}$ radicals production. Transient absorption spectroscopy experiments revealed the occurrence of an alternative oxidation pathway involving the valence band holes and yielded relevant kinetic information related to the early stages of the As(III) photooxidation. The higher absorption of the electron–hole pairs observed for the samples treated at lower temperature means that controlling the pyrolysis temperature during the synthesis of the Fe–Cu nanocomposites allows tuning the photocatalyst activity for oxidation of substrates via valence band holes, or via $HO^{\cdot}$ radicals.

Graphical abstract

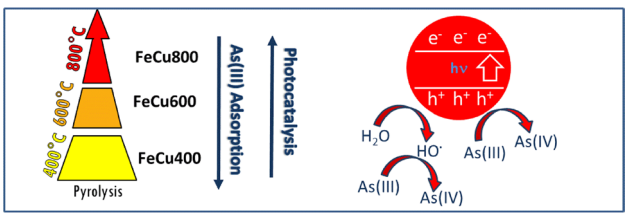

Keywords Photocatalysis · Arsenic · Iron-copper nanocomposites · Photooxidation · Transient absorption spectroscopy

This paper is part of the Special Issue dedicated to Prof. Silvia E. Braslavsky on the occasion of her 80th birthday.

✉ Luciano Carlos
luciano.carlos@probien.gob.ar

✉ Daniel O. Mártire
dmartire@inifta.unlp.edu.ar

[1] Instituto de Investigaciones Fisicoquímicas Teóricas y Aplicadas (INIFTA), Departamento de Química, Facultad de Ciencias Exactas, Universidad Nacional de la Plata, CONICET, Casilla de Correo 16, Sucursal 4, 1900 La Plata, Argentina

[2] Department of Chemistry and Bioscience, Aalborg University, Fredrik Bajers Vej 7H, 9220 Aalborg, Denmark

[3] Dipartimento di Chimica and NIS Inter-Departmental Centre, Università di Torino, Via Pietro Giuria 7, 10125 Torino, Italy

[4] Instituto de Investigación y Desarrollo en Ingeniería de Procesos, Biotecnología y Energías Alternativas, PROBIEN (CONICET-UNCo), Universidad Nacional del Comahue, 8300 Neuquén, Argentina

1 Introduction

Arsenic contamination in groundwater is widely recognized as a global health problem. About 137 million people in more than 70 countries are affected by high levels of arsenic in everyday drinking water. The fact that it is present in the atmosphere, soil, rocks, bodies of water, minerals, in its inorganic, organic, and methylated form, is a proof of its easy mobilization under natural conditions. In addition, various large-scale activities such as mining, the use of fossil fuels, organic pesticides and herbicides, and agricultural desiccants have been introducing an increasing number of toxic forms of arsenic in the environment. Arsenic is also used as a food additive for livestock and poultry [1]. As a consequence of natural geological and anthropogenic contamination, high levels of arsenic can be found in groundwater in numerous places of Argentina, Bangladesh, China, Chile, Mexico, India, Taiwan, Mongolia, and the United States of North America [2].

Arsenic can undergo oxidation–reduction, precipitation–dissolution, adsorption–desorption reactions, as well as organic and biochemical methylation, depending on environmental and biological conditions. The toxicity of arsenic species depends on the oxidation state, speciation, availability, and the animal species or cell types exposed. As(III) is considerably more toxic than the As(V), due to its greater capacity to bind to thiols of biomolecules, such as lipoic acid and protein cysteine residues [3]. The bioavailability of As is determined mainly by speciation. Therefore, the oxidation of As(III) to As(V) is beneficial for the effective remediation of arsenic [4]. Depending on pH, As(III) in aqueous solution mainly exists as H_3AsO_3, $H_2AsO_3^-$, $HAsO_3^{2-}$ and/or AsO_3^{3-} and As(V) as H_3AsO_4, $HAsO_4^{2-}$ and/or AsO_4^{3-} [3–6].

Heterogeneous photocatalysis on TiO_2 was proposed as a promising advanced oxidation technology for the treatment of arsenic contaminated water [7]. This photocatalyst has a high oxidation efficiency, chemical stability, non-toxicity, availability, and low cost [8]. However, TiO_2 nanoparticles are often immobilized on inert substrates to allow their recovery, but this approach reduces the number of active sites on the catalyst, leading to a decrease in the photocatalytic effectiveness [9].

The incorporation of magnetic nanophotocatalysts (MNPCs) in water treatment technologies has recently received much attention due to the fact that magnetic separation is an environmentally friendly method for the recovery of nanomaterials [10].

MNPCs have large specific surface area, chemical stability, and a high degradation efficiency, which would imply lower doses and faster kinetics compared to conventional catalysts, reducing the costs of the process. The outstanding potential of these materials makes them suitable for many reactions in both liquid and gas phases [11]. In particular, γ-Fe_2O_3–TiO_2 magnetic nanoparticles were employed to remove arsenite through simultaneous photocatalytic oxidation and adsorption [12].

We have recently prepared magnetic Fe–Cu nanocomposites with photocatalytic applications via the precursors method, employing lignin-derived bio-based substances (BBS) isolated from the compost of organic fraction of urban wastes as complexing agent for the Fe^{3+} and Cu^{2+} ions in the precursors. [13]. This synthesis procedure consisted in the thermal decomposition under N_2 atmosphere of dried complex-precursors formed via the reaction of Fe^{3+} and Cu^{2+} salts with carboxylate and O-alkyl groups of BBS. The excellent photocatalytic performance of the nanocomposites was assigned to the formation of γ-Fe_2O_3/Cu_2S and γ-Fe_2O_3/CuS heterojunctions via the Z-scheme mechanism. The ability of the Fe–Cu nanocomposites to generate $HO^{\cdot}$ radicals upon photoirradiation was proven by electron paramagnetic resonance (EPR) spectroscopy and they were successfully employed as photocatalysts for the degradation of carbamazepine, one of the most often detected pharmaceuticals in aquatic systems [13]. The use of BBS as coating of magnetite nanoparticles for technological and environmental applications, such as adsorbents [14] and photocatalysts [15], contributes to reducing the environmental impact of urban waste.

Here, we tested three of these magnetic Fe–Cu bimetallic nanocomposites as MNPCs for the adsorption and photocatalytic oxidation of As(III). These nanocomposites were prepared with the same amount of BBS and subjected to thermal treatment at different temperatures [13]. Transient absorption spectroscopy experiments yielded information on the early stages involved in the photocatalyzed oxidation of As(III). The results obtained here show how arsenic contaminated water can be remediated using photocatalysts prepared from the organic fraction of urban wastes.

1.1 Materials and methods

2 Materials

$NaAsO_2$, $Na_2HAsO_4{\cdot}7H_2O$, $FeCl_3{\cdot}6H_2O$, $CuSO_4$, KSCN, triethanolamine (TEOA), and acetonitrile were purchased from Sigma Aldrich. Ascorbic acid was obtained from Carlo Erba Pharma, potassium antimonyl tartrate trihydrate ($C_8H_4K_2O_{12}Sb_3{\cdot}H_2O$), and aqueous NH_3 (26–30%) were from Biopack. Ammonium molybdate $(NH_4)_6Mo_7O_{24}{\cdot}4H_2O$ and $FeSO_4{\cdot}7H_2O$ were from Merck. Absolute ethanol and H_2SO_4 were from Cicarelli. Iron (III) acetylacetonate, $Fe(acac)_3$, was purchased from Fluka. The BBS employed

in this study was derived from 230 days of composting of green refuse (at Acea Pinerolese plant at Pinerolo, Torino, Italy) and was processed at the pilot plant of Studio Chiono e Associati at Rivarolo Canavese, Torino, Italy. The extraction procedure of BBS as well as its physicochemical characterization was already reported elsewhere [16]. In brief, BBS are biological macromolecules with a complex lignin-derived structure containing several functional groups, such as COOH, CON, CO, PhOH, and O-alkyl, bonded to aromatic and aliphatic chains. The chemical composition of BBS is shown in Table S1, in the Supplementary Information.

2.1 Synthesis of the Fe–Cu nanocomposites

The procedure was previously reported [13]. A volume of 150 mL of an aqueous solution containing Fe^{3+} (0.15 M), Cu^{2+} (0.15 M), and BBS (0.9 wt%) was stirred in a closed beaker at room temperature for 24 h. Then, after 10 min centrifugation at 4000 rpm, the separated solid (precursor complexes) was dried in an oven at 60 °C until constant weight. The precursor complexes of the nanocomposites contained 17.0 wt% Fe, 10.0 wt% Cu, and 65.5 % OM. The dried solid was placed in a tubular furnace and heated at a rate of 2 °C min^{-1} under N_2 atmosphere (2 mL min^{-1}) from room temperature up to the desired temperature (400, 600, or 800 °C). The resulting materials, named FeCu400, FeCu600, and FeCu800, were magnetically separated from the supernatant and the solid was washed with deionized water. Finally, the solid was dried and stored at room temperature. Table 1 shows the specific surface area (SSA), organic matter (OM) content, and elemental composition of the nanocomposites.

2.2 Steady-state irradiation assays

All continuous irradiation experiments were carried out in a septum-capped quartz cell located in the center of the RPR Rayonet reactor equipped with 8 lamps with a centered emission at 350 nm (see Figure S1 in the Supplementary Information). The photon flux per sample unit volume ($P_0 = 3.5 \times 10^{-5}$ Einstein L^{-1}) was measured using potassium ferrioxalate as an actinometer [17]. A sample volume of 2 mL containing 0.125 g L^{-1} of the nanocomposites and 225 ppm of As(III) was irradiated for 60 min. After irradiation, the nanocomposites were magnetically separated and then filtered to ensure the extraction of small suspended particles.

Table 1 Specific surface area (SSA), OM content, and elemental composition of the magnetic nanomaterials

Sample	($m^2 g^{-1}$)	OM[b] (wt%)	C[c] (wt%)	N[c] (wt%)	S[c] (wt%)
FeCu400	33	36.9	26.23	3.60	4.90
FeCu600	138	n.d.[d]	9.78	3.38	11.90
FeCu800	158	n.d.[d]	10.60	2.15	9.32

[a]BET model

[b]TGA analysis

[c]Elemental analysis

[d]Not estimated (see text)

2.3 Laser flash-photolysis (LFP)

In order to obtain information about the participation of electron–hole pairs in the reaction mechanism, an LP980 laser flash-photolysis from Edinburgh instruments was employed. The third harmonic (355 nm) of a Continuum Surelite Nd:YAG laser (20 ns fwhm) was the excitation source. Decay-associated difference spectra (DADS) were performed by application of global analysis with the free software program Glotaran [18].

2.4 Determination of total As

For measuring total As, a commercial kit from MQuant was used. The kit senses As(III) and As(V), without distinguishing between them. The total arsenic concentration is determined by visual comparison of the reaction zone of the test strip with a colorimetric scale included in the kit. The procedure involves the addition of Zn powder, a solid acid, and an oxidant to remove interfering sulfide ions. Zn reduces arsenic (III) and arsenic (V) compounds to arsine (AsH_3), which reacts with $HgBr_2$ contained in the reaction zone of the test strip, to yield yellow-brown halides of arsenic and mercury.

2.5 Measurement of As(V) concentration

The colorimetric method originally used to quantify phosphate ions can be applied for the determination of arsenic in the absence of phosphates [19]. To prepare the colorimetric reagent, solutions of the components were added in the following order: 5 mL of 2.5 M H_2SO_4, 0.5 mL of potassium antimonyl tartrate, 1.5 mL ammonium molybdate, and finally 3 mL of 0.1 M ascorbic acid. A volume of 0.8 mL of the colorimetric reagent was then mixed with 5 mL of the sample. The absorbance was measured at 850 nm after 30 min of starting the reaction with a T90 + UV/Vis instrument (PG Instruments Ltd.).

3 Results and discussion

The nanocomposites were characterized in our previous paper [13]. In order to be able to discuss the results obtained here, we will briefly summarize some of the most relevant

physicochemical properties related to their adsorption and photocatalytic performance.

From XANES data, it was possible to simulate the experimental spectra at the Fe K-edge of the nanocomposites using a linear combination of different contributions of reference spectra [13]. The best fitting for the FeCu400 was obtained for 60% Fe_3O_4, 20% α-Fe_2O_3, and 20% γ-Fe_2O_3. For FeCu600/1 sample, the best results were obtained with a combination of Fe_3O_4 (61%), γ-Fe_2O_3 (18%) and α-Fe2O3 (21%). For FeCu800/1, 65% is made of Fe_3O_4, 20% of γ-Fe_2O_3 and 15% of Fe^0. The spectra at the Cu K-edge for FeCu400 were well reproduced with a linear combination of the spectrum of copper ion complexed with BBS (77%) and Cu2S reference (23%). For the FeCu600/1 sample, the main phase seems to be Cu_2S (52%), whereas in the FeCu800/1 sample, the main phase is CuS (47%).

The adsorption–desorption isotherms of N_2 at 77 K previously measured [13] showed that the three nanocomposites present type IV isotherms according to the IUPAC classification, which are typical of mesoporous materials. The corresponding values of SSA are shown in Table 1. Concerning the characterization of the nanocomposites as photocatalysts, in our previous paper, we showed direct evidence of the generation of hydroxyl radicals upon irradiation of suspensions of the nanomaterials with a solar simulator via EPR spectroscopy using the spin-trapping approach. All three nanocomposites showed the characteristic EPR spectra of the DMPO-OH spin adduct, which confirms the generation of hydroxyl radicals. Similar intensities of the EPR signal were obtained for FeCu400 and FeCu600, whereas the intensity of the FeCu800 signal was almost twice as high.

All these results motivated the investigation of the performance of the nanocomposites as adsorbents of As(III) and as photocatalysts for As(III) oxidation.

3.1 Steady-state photoirradiation experiments

Figure 1 shows the total concentration of As after treatment of the samples with the nanocomposites under different conditions, in the dark, and under steady-state irradiation.

For data obtained in the dark, the total concentration of As in solution significantly decreases after being in contact with the nanocomposites. In particular, the amount of sorbed As per gram of nanocomposite (q, mg g^{-1}) after 1 h of contact were 911, 840, and 200 mg g^{-1}, for FeCu400, FeCu600, and FeCu800, respectively. In fact, the amount of sorbed As(III) per gram of FeCu400 and FeCu600 are higher than the highest value reposted for any adsorbent, namely 416 mg g^{-1} for carbon nanosphere–iron oxide nanocomposites [20]. The trend of the adsorption capacities FeCu400 ≈ FeCu600 > FeCu800 is not expected from the SSA values, which increase with the treatment temperature (see Table 1). The lower intensity of the signals assigned to carboxylic-OH

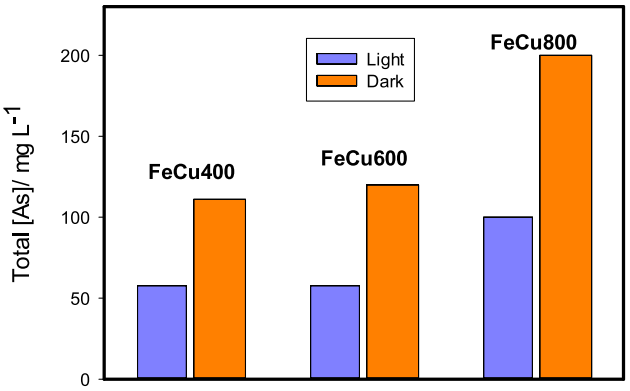

Fig. 1 Remnant total arsenic concentration after 1 h contact of the air-saturated samples of the nanocomposites (0.125 g L^{-1}) with 225 ppm of As(III) in the dark and under photoirradiation

(3408 cm^{-1}) and carboxylate COO^- asymmetric stretching (1615 cm^{-1}) groups in the FTIR spectrum of FeCu800 [13] is indicative of a lower concentration of carboxylic groups in FeCu800 compared to FeCu400 and FeCu600. These functional groups play an important role in the complexation between humic-like substances, such as BBS, and arsenite [21]. Thus, we assign the better performance of FeCu400 and FeCu600 compared to FeCu800 to the higher concentration of carboxylic groups in these samples. We should also consider that As(III) can be adsorbed on magnetite via the formation of different types of complexes [22].

Photoirradiation produces a decrease in the amount of total arsenic in the supernatant after the magnetic separation of the particles. This indicates that the products generated in the photocatalytic process do not remain largely in solution, in complete agreement with the reported higher adsorption affinity of As(V) species compared to As(III) [5]. The largest difference in total arsenic concentration between irradiated and non-irradiated samples is found for FeCu800 (see Fig. 1). According to this result, the best photocatalyst for the oxidation of As(III) is FeCu800. This nanocomposite produces the highest concentration of $HO^{\cdot}$ radicals upon irradiation [13]. Therefore, we propose the involvement of this species in the reaction mechanism, as already reported for the TiO_2-photocatalyzed oxidation of As(III) [23, 24].

The excellent photocatalytic performance of the FeCu600 and FeCu800 nanocomposites, in our previous paper, was assigned to a Z-scheme mechanism between the iron oxides (either α-Fe_2O_3 or γ-Fe_2O_3) and the copper sulfides (either Cu_2S or CuS). In this mechanism when both semiconductors are excited by incident light, the photogenerated holes in α-Fe_2O_3 or γ-Fe_2O_3 and the electrons in CuS or Cu_2S, maintain their reduction and oxidation potential because the CB electrons of α-Fe_2O_3 or γ-Fe_2O_3 with a lower reduction potential than those in CuS or Cu_2S, recombine with holes on the copper sulfides, with lower oxidation potentials than

those in α-Fe_2O_3 or γ-Fe_2O_3. This scheme explains the generation of hydroxyl radicals via water oxidation by the iron oxides holes [13].

The concentration of As(V) was measured in the supernatant after irradiation under air and Ar-saturation (Fig. 2). For all the nanocomposites, the concentration of As(V) is larger when the irradiation takes place under air-saturation conditions than under Ar-atmosphere. This is an expected result because in the presence of air, O_2 works as a trap for the electrons of the conduction band (e_{cb}^-), giving rise to the formation of the superoxide radical anion ($O_2^{\cdot -}$, Eq. 1).

$$O_2 + e^- \rightarrow O_2^{\cdot -} \quad (1)$$

Under these conditions, the lifetime of the holes is prolonged. Since the valence band holes are likely to be either the species directly involved in the oxidation of As(III) or the precursors of other oxidizing species such as the $HO^{\cdot}$ radicals [25], the presence of O_2 should favor the oxidative pathways not mediated by the triplet states of the organic matter, and thus larger amounts of As(V) are formed. Even in the absence of nanocomposites, the formation of a low concentration of As(V) (0.5 mg L^{-1} in air-saturated conditions) is formed. The uncatalyzed photooxidation of arsenite to arsenate was previously studied by Ryu et al. [26] These authors reported a large quantum yield at a wavelength of 254 nm, where arsenite has a very low molar absorption coefficient. Under our excitation conditions (350 nm), the absorption coefficient of arsenite is still much lower and this may be one of the reasons for the very low concentration of As(V) detected in the absence of photocatalysts. The fact that the lowest concentration of As(V) in solution was measured for the best photocatalyst (FeCu800) indicates that once As(V) is formed, it remains adsorbed on the surface of the nanocomposite.

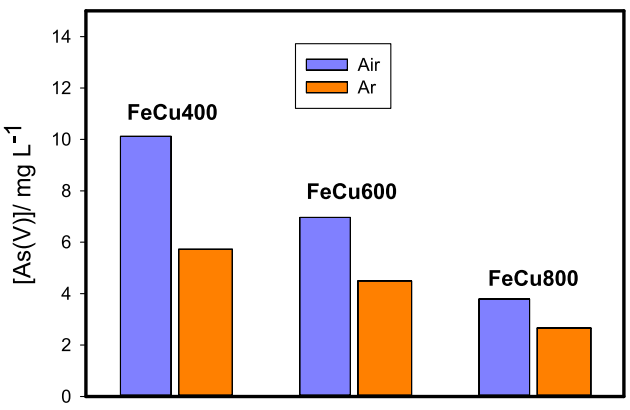

Fig. 2 Concentration of As(V) measured for the photoirradiation experiments of Fig. 1. Air and Argon refer to irradiation experiments under different atmospheres

3.2 Charge-separated states of electron–hole pairs detected by laser flash-photolysis (LFP)

To obtain additional information on the reaction mechanism, transient absorption assays were performed. Transient techniques provide a very sensitive means of understanding the charge carrier dynamics. The experiments were performed with samples FeCu400, FeCu600, and FeCu800 in order to investigate the effect of the temperature treatment on the semiconductor performance of the nanomaterials. LFP experiments were performed with Ar-saturated suspensions of the nanomaterials at a concentration of 2.5 g L^{-1}. All samples showed the decay of transient species in the whole range of analysis wavelengths (370–750 nm). Two typical signals obtained for suspensions of FeCu400 at 605 and 455 nm are shown in Fig. 3a, b.

From comparison of the spectra obtained at different times after the laser shot (see Fig. 3c) with those reported for various families of semiconductor nanoparticles [27], we can assign the observed transients to electron–hole pairs. In order to elucidate whether more than one component contributes to the absorbance signals, a global analysis was performed with the Glotaran software. As can be seen in Table 1, for all the samples, there is a short lifetime of the same order of magnitude as the laser pulse, which can be related to the response of the detection system to light scattering. The second component of longer lifetime is assigned to charge-separated states of electron–hole pairs located in different traps.

In order to complete the characterization of the charge-separated states, two different scavengers of holes were employed in LFP experiments: KSCN and TEOA [28, 29]. Transient absorption spectra for samples of FeCu400, FeCu600, and FeCu800 obtained in the absence and presence of 0.05 M KSCN were coincident (see Fig. 3c, d for FeCu400). For the three nanocomposites, the decay of longer-lived species obtained from the program is faster in the presence of KSCN (Table 1). Table 1 also shows the corresponding quenching rate constants k_q, which are well below the diffusion-controlled limit. It is noteworthy that the absorption of the charge-separated states of electron–hole pairs precludes the observation of the absorption of dithiocyanate radical anions ($\lambda^{max} = 475$ nm), which are expected to be formed by Eqs. 2 and 3 [30].

$$\text{Trapped } h^+ + SCN^- \rightarrow SCN^{\cdot} \quad (2)$$

$$SCN^{\cdot} + SCN^- \rightleftarrows (SCN)_2^{\cdot -} \quad (3)$$

Similar results were obtained by Bahnemann et al. with the TiO_2 photocatalyst [28]. These authors used nanosecond flash photolysis to study hole scavenging by thiocyanate and dichloroacetate and concluded that some holes react with the

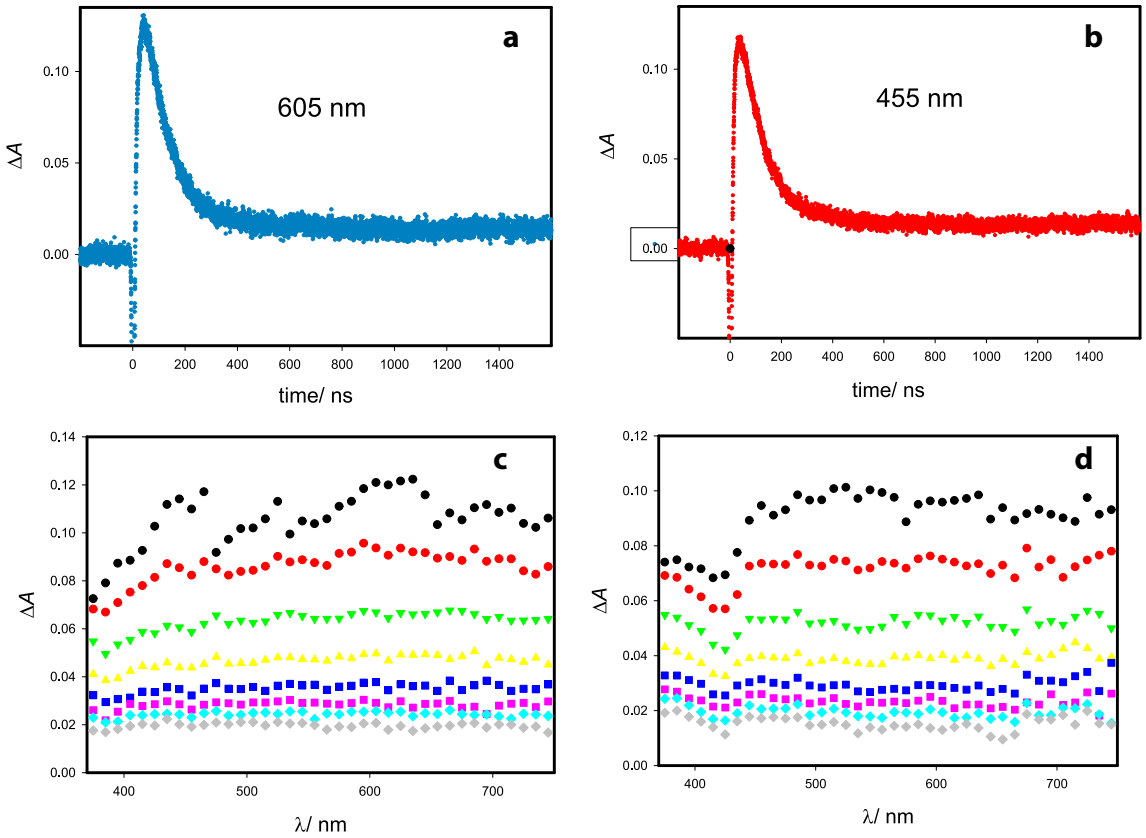

Fig. 3 Absorbance profiles obtained after laser excitation of Ar-saturated 2.5 g L^{-1} suspensions of FeCu400 at 605 nm (**a**) and 455 nm (**b**). Difference absorption spectra of the transient species obtained at different times after the laser shot: in the absence (**c**) and presence of 0.05 M KSCN (hole scavenger) (**d**). The spectra shown in pictures **c**, **d** correspond from top to bottom to the following times after the laser shot: 0, 40, 80, 120, 160, 200, 240, and 320 ns

adsorbed hole scavengers promptly within the duration of the laser pulse (20 ns), and others react more slowly. Ultrafast pump-probe spectroscopy studies confirm that for the thiocyanate anion, the prompt reaction occurs on the femtosecond time scale, whereas some holes react more slowly and others do not react at all, at any concentration of the hole scavenger [28]. Based on these reports, the quenching effect observed here (Table 2) can be assigned to the holes reacting slowly with thiocyanate ions.

In order to achieve accumulation of electrons, 4:1 mixtures of acetonitrile and triethanolamine (TEOA) in volume were employed as the solvent [29, 31]. Under these conditions, TEOA scavenges the holes according to Eq. 4.

$$\text{Trapped } h^+ + \text{TEOA} \rightarrow \text{TEOA}^{\cdot+} \quad (4)$$

Figure 4 shows the spectra taken immediately after the laser shot with Ar-saturated samples of FeCu400, FeCu600, and FeCu800 in 4:1 acetonitrile:TEOA. As can be seen in the spectra, the transient absorption is larger in the longer wavelength region (> 650 nm, related to the absorption of electrons) than in the shorter wavelength region (related to trapped holes). Similar results were reported by Ma et al. [32] who performed nanosecond LFP experiments with aqueous suspensions of other semiconductors. The shorter wavelength band of the absorption spectrum of the charge-separated states was suppressed upon the addition of glycerol as an efficient hole scavenger. Based on these reported results, we conclude that the main contribution to the absorption spectrum shown in Fig. 4 is due to electrons trapped in the nanocomposites. The intensity of the

Table 2 Lifetimes (τ) of the species retrieved from the Glotaran software for the LFP experiments performed with Ar-saturated suspensions of the nanomaterials in the absence and presence of 0.05 M KSCN

Nanomaterial	Lifetimes without KSCN		Lifetimes with 0.05 M KSCN		k_q (M^{-1} s^{-1})
	τ_1 (ns)	τ_2 (ns)	τ_1 (ns)	τ_2 (ns)	
FeCu400	5.5	301	7.1	222	2.4×10^7
FeCu600	7.3	289	6.9	261	2.1×10^7
FeCu800	4.4	458	5.8	284	2.7×10^7

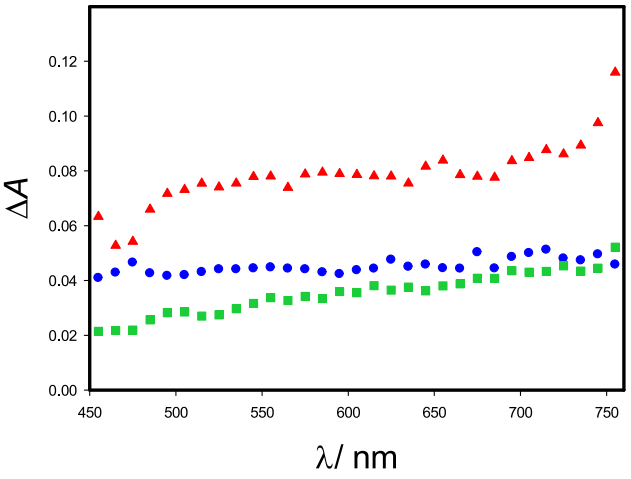

Fig. 4 Difference absorption spectra of taken immediately after the laser shot with Ar-saturated 0.25 g L^{-1} suspensions of FeCu400 (red), FeCu600 (blue), and FeCu800 (green) in 4:1 acetonitrile: TEOA

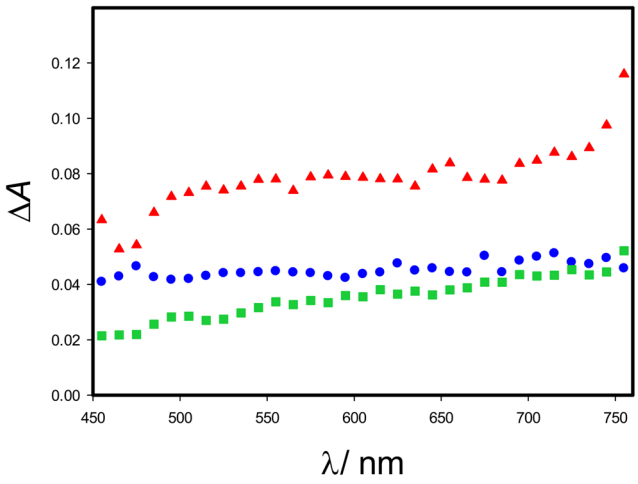

Fig. 5 Differential absorption spectra of the electron–hole pair obtained by LFP of Ar-saturated aqueous samples containing 0.5 g L^{-1} of FeCu400 and 0.5 mM As(III). The spectra were taken, from top to bottom, at the following times after the laser shot: 0, 40, 80, 120, 160, 200, 240, and 320 ns

absorbance immediately after the laser shot follows the trend FeCu400 > FeCu600 > FeCu800. This means that more electron–hole pairs are generated for the samples treated at lower temperatures. For these samples, the Glotaran program yielded only one component with lifetimes 220, 138, and 269 ns, for FeCu400/1, FeCu600/1 and FeCu800/1, respectively.

3.3 Laser flash-photolysis (LFP) experiments in the presence of As(III)

The results shown in the previous section confirm the assignment of the observed transient species to charge-separated states of electron–hole pairs. In order to better understand the early stages mechanism of As(III) oxidation, LFP assays were performed with FeCu400. FeCu400 was chosen because this nanocomposite showed the highest transient absorption in assays performed in the absence of As(III).

The shape of the absorption spectra at different times after the laser pulse obtained from experiments performed in the presence of As(III) (Fig. 5) are similar to those obtained in the absence of As(III) (Fig. 3c), although a more pronounced absorption is observed in the 600- 650 nm range.

To evaluate the effect of the concentration of As(III) on the transient species kinetics, LFP assays were performed in Ar-saturated samples containing 0.5 g L^{-1} FeCu400 and As(III) in the concentration range 0–5 mM. The amplitude of the signals at 620 nm increases with increasing concentration of As(III) (Fig. 6a). The signal decay also depends on the concentration of As(III). As shown in Fig. 6b, the decay rate constant (k_{dec}), obtained from fitting the decays to a single exponential function (see red lines in Fig. 6a), increases with the concentration of As(III) up to ca. 3 mM, where it reaches a plateau.

The dependence of k_{dec} on [As(III)] can be interpreted by assuming that the oxidation of As(III) to As(IV) is mediated by the holes generated in the valence band of the photocatalyst. Then, it is expected that under conditions where the holes are scavenged, the holes-mediated oxidation should be strongly inhibited. To validate this hypothesis, LFP tests were carried out in a 50% water–ethanol solution, using ethanol as a hole scavenger [33]. Under these conditions, it was verified that there is no effect of the As(III) concentration on the decay rate of the electron–hole pair (see Figure S2 in the Supplementary Information). This result is due to the fact that those holes that were accessible to react with As(III) in the absence of ethanol are now no longer available because they have been sequestered by the alcohol. Thus, the participation of the holes in the early stages of As(III) photocatalyzed by FeCu400 is confirmed.

3.4 Reaction mechanism of the photocatalyzed oxidation of As(III)

The reaction mechanism outlined in Eqs. 5 to 7, which reproduces the behavior shown in Fig. 6b, can explain the initial stages of the photocatalyzed oxidation of As(III).

$$\text{FeCu400} \xrightarrow{h\nu} (h^+ + e^-) \quad (5)$$

$$(h^+ + e^-) \xrightarrow{H_2O,\, k_1} \text{Products} \quad (6)$$

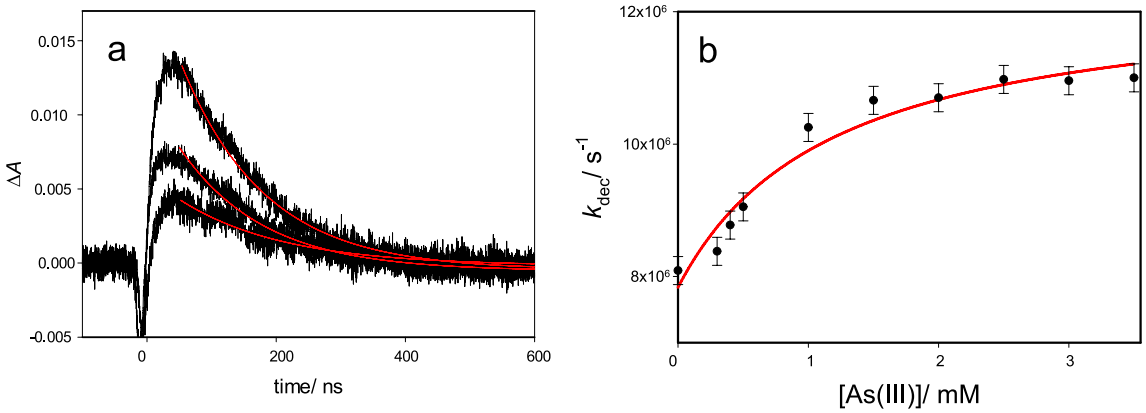

Fig. 6. **a** Absorbance decays obtained at 620 nm after laser excitation of Ar-saturated aqueous samples containing 0.5 g L^{-1} of FeCu400 and different As(III) concentrations (from bottom to top): 0.5; 1.0, and 4.0 mM. **b** Decay constant k vs. [As(III)] concentration. The red line corresponds to the non-linear fit of the data to Eq. 8

$$(h^+ + e^-) + As(III) \overset{K}{\leftrightarrows} C \xrightarrow{k_2} As(IV) + e^- \quad (7)$$

After generation of the electron–hole pair ($(h^+ + e^-)$ in Eq. 5), it can either decay by reaction with the solvent (Eq. 6) or it can react with As(III) to reversibly form a 1:1 complex C, which decomposes to yield As(IV) species (Eq. 7). The increase in signal intensity in the presence of As(III) (Fig. 6a) reveals that complex C has an absorption coefficient larger than the uncomplexed electron–hole pair in the 600–650 nm range. Assuming a pre-equilibrium condition between the holes, As(III) and complex C, Eq. 8 is obtained for the decay of the electron–hole pairs. The derivation of Eq. 8 is given in the Supplementary Information.

$$k_{dec} = \frac{k_1 + k_2 \times K \times [As(III)]}{1 + K \times [As(III)]} \quad (8)$$

The values of $k_1 = 7.8 \pm 0.3 \times 10^6$ s^{-1}, $k_2 = 1.2 \pm 0.5 \times 10^{10}$ s^{-1}, and $K = 1.1 \pm 0.3 \times 10^3$ were obtained from the nonlinear fitting of the experimental data to Eq. 8 (see red line in Fig. 6b).

The correlation between the results of our steady-state experiments (Fig. 1) with the production of $HO^{\cdot}$ radicals [13] clearly indicates the involvement of this species in the oxidation of As(III) photocatalyzed by the nanocomposites. However, as unambiguously shown by the transient absorption experiments, the valence band holes are also involved in the reaction mechanism. One reason for the reported generation of lower amounts of $HO^{\cdot}$ radicals upon irradiation of the samples treated at lower temperature is the high content of C=C aromatic species, which are efficient hydroxyl radical scavengers [13]. Thus, although according to our transient absorption experiments, more electron–hole pairs are formed when FeCu400 is photoirradiated, probably resulting in a higher initial concentration of $HO^{\cdot}$ radicals, most of these radicals are scavenged by the organic matter and therefore, are neither detected in the EPR experiment nor available for the As(III) oxidation.

4 Conclusion

We have here shown that the three tested magnetic Fe–Cu nanocomposites, prepared by using soluble substances isolated from urban biowaste as carbon sources under different temperature of the pyrolysis treatment (400, 600, and 800 °C) showed adsorption capacities of As(III) higher than the highest value reported for any adsorbent. All three nanocomposites photocatalyzed the oxidation of As(III). The trend of photocatalytic performance FeCu400 < FeCu600 < FeCu800 is in complete agreement with the ability of the nanocomposites to generate $HO^{\cdot}$ radicals, as measured by EPR spectroscopy.

Transient absorption experiments also confirmed the involvement of the valence band holes in the early stages of the As(III) photooxidation. In addition, the higher absorption of the electron–hole pairs observed for the samples treated at lower temperature means that controlling the pyrolysis temperature during the synthesis of the Fe–Cu nanocomposites allows tuning the photocatalyst activity for oxidation of substrates via valence band holes, or via $HO^{\cdot}$ radicals.

Supplementary Information The online version contains supplementary material available at https://doi.org/10.1007/s43630-022-00330-z.

Acknowledgements This project has received funding from the European Union's Horizon 2020 research and innovative program under the Marie Sklodowska-Curie Grant agreement no. 645551 and from ANPCyT, Argentina (PICT 2016-0974, PICT 2017-1628, and PICT 2019-03140). L. Morán Ayala and F. Aparicio thank CONICET for their research graduate grants. L. Carlos and G. Bosio are research

members of CONICET (Argentina). D. Mártire is a research member of CIC (Buenos Aires, Argentina).

Declarations

Conflict of interest There are no conflicts of competing interest to declare.

References

1. Alam, M. S., Wu, Y., & Cheng, T. (2014). Silicate minerals as a source of arsenic contamination in groundwater. *Water Air Soil Pollution, 225*, 1–15. https://doi.org/10.1007/S11270-014-2201-9
2. Shaji, E., Santosh, M., Sarath, K. V., Prakash, V., Deepchand, P., & Divya, B. V. (2021). Arsenic contamination of groundwater: A global synopsis with focus on the Indian Peninsula. *Geoscience Frontier, 12*, 101079. https://doi.org/10.1016/j.gsf.2020.08.015
3. Pham, P., Rashid, M., Cai, Y., Yoshinaga, M., Dionysiou, D. D., & O'Shea, K. (2020). Removal of As(III) from water using the adsorptive and photocatalytic properties of humic acid-coated magnetite nanoparticles. *Nanomaterials, 10*, 1604. https://doi.org/10.3390/NANO10081604
4. Bhandari, N., Reeder, R. J., & Strongin, D. R. (2011). Photoinduced oxidation of arsenite to arsenate on ferrihydrite. *Environmental Science and Technology, 45*, 2783–2789. https://doi.org/10.1021/es103793y
5. Gillispie, E. C., Sowers, T. D., Duckworth, O. W., & Polizzotto, M. L. (2015). Soil pollution due to irrigation with arsenic-contaminated groundwater: current state of science. *Current Pollution Reports, 1*, 1–12. https://doi.org/10.1007/s40726-015-0001-5
6. Mondal, P., Majumder, C. B., & Mohanty, B. (2006). Laboratory based approaches for arsenic remediation from contaminated water: Recent developments. *Journal of Hazardous Materials, 137*, 464–479. https://doi.org/10.1016/J.JHAZMAT.2006.02.023
7. Litter, M. I. (2015). Mechanisms of removal of heavy metals and arsenic from water by TiO_2-heterogeneous photocatalysis. *Pure Applied Chemistry, 87*, 557–567. https://doi.org/10.1515/PAC-2014-0710/PDF
8. Gupta, S. M., & Tripathi, M. (2011). A review of TiO_2 nanoparticles. *Chinese Science Bulletin, 56*, 1639–1657. https://doi.org/10.1007/S11434-011-4476-1
9. Ahmad, R., Ahmad, Z., Khan, A. U., Mastoi, N. R., Aslam, M., & Kim, J. (2016). Photocatalytic systems as an advanced environmental remediation: Recent developments, limitations and new avenues for applications. *Journal of Environmental Chemistry and Engineering, 4*, 4143–4164. https://doi.org/10.1016/j.jece.2016.09.009
10. Peralta, M. E., Ocampo, S., Funes, I. G., Medina, F. O., Parolo, M. E., & Carlos, L. (2020). Nanomaterials with tailored magnetic properties as adsorbents of organic pollutants from wastewaters. *Inorganics, 8*, 1–25. https://doi.org/10.3390/inorganics8040024
11. Ibhadon, A. O., & Fitzpatrick, P. (2013). Heterogeneous photocatalysis: Recent advances and applications. *Catalysis, 3*, 189–218. https://doi.org/10.3390/CATAL3010189
12. Yu, L., Peng, X., Ni, F., Li, J., Wang, D., & Luan, Z. (2013). Arsenite removal from aqueous solutions by γ-Fe_2O_3-TiO_2 magnetic nanoparticles through simultaneous photocatalytic oxidation and adsorption. *Journal of Hazardous Materials, 246–247*, 10–17. https://doi.org/10.1016/J.JHAZMAT.2012.12.007
13. Aparicio, F., Mizrahi, M., Ramallo-López, J. M., Laurenti, E., Magnacca, G., Carlos, L., & Mártire, D. O. (2022). Novel bimetallic magnetic nanocomposites obtained from waste-sourced bio-based substances as sustainable photocatalysts. *Materials Research Bulletin*. https://doi.org/10.1016/j.materresbull.2022.111846
14. Magnacca, G., Allera, A., Montoneri, E., Celi, L., Benito, E., Gagliardi, L. G., Gonzalez, C., Martire, D. O., & Carlos, L. (2014). Novel magnetite nanoparticles coated with waste-sourced biobased substances as sustainable and renewable adsorbing materials. *ACS Sustainable Chemistry and Engineering, 2*(6), 1518–1524. https://doi.org/10.1021/sc500213j
15. Franzoso, F., Nisticò, R., Cesano, F., Corazzari, I., Turci, F., Scarano, D., Bianco Prevot, A., Magnacca, G., Carlos, L., & Mártire, D. O. (2017). Biowaste-derived substances as a tool for obtaining magnet-sensitive materials for environmental applications in wastewater treatments. *Chemical Engineering Journal, 310*, 307–316. https://doi.org/10.1016/j.cej.2016.10.120
16. Gomis, J., Vercher, R. F., Amat, A. M., Mártire, D. O., González, M. C., Bianco Prevot, A., Montoneri, E., Arques, A., & Carlos, L. (2013). Application of soluble bio-organic substances (SBO) as photocatalysts for wastewater treatment: Sensitizing effect and photo-Fenton-like process. *Catalysis Today, 209*, 176–180. https://doi.org/10.1016/j.cattod.2012.08.036
17. Aparicio, F., Escalada, J. P., De Gerónimo, E., Aparicio, V. C., Einschlag, F. S. G., Magnacca, G., Carlos, L., & Mártire, D. O. (2019). Carbamazepine degradation mediated by light in the presence of humic substances-coated magnetite nanoparticles. *Nanomaterials, 9*, 1–12. https://doi.org/10.3390/nano9101379
18. Snellenburg, J. J., Laptenok, S., Seger, R., Mullen, K. M., & van Stokkum, I. H. M. (2012). Glotaran: A Java-based graphical user interface for the R package TIMP. *Journal of Statistical Software, 49*, 1–22. https://doi.org/10.18637/JSS.V049.I03
19. Pecini, E. M., Springer, V., Brigante, M., & Avena, M. (2017). Arsenate interaction with the surface of nanomagnetic particles. High adsorption or full release. *Journal of Environmental Chemical Engineering, 5*, 4917–4922. https://doi.org/10.1016/j.jece.2017.09.020
20. Su, H., Ye, Z., Hmidi, N., & Subramanian, R. (2017). Carbon nanosphere–iron oxide nanocomposites as high-capacity adsorbents for arsenic removal. *RSC Advances, 7*, 36138–36148. https://doi.org/10.1039/C7RA06187K
21. Gong, X. J., Li, Y. S., Dong, Y. Q., & Li, W. G. (2020). Arsenic adsorption by innovative iron/calcium in-situ-impregnated mesoporous activated carbons from low-temperature water and effects of the presence of humic acids. *Chemosphere, 250*, 126275. https://doi.org/10.1016/j.chemosphere.2020.126275
22. Nisticò, R., Celi, L. R., Bianco Prevot, A., Carlos, L., Magnacca, G., Zanzo, E., & Martin, M. (2018). Sustainable magnet-responsive nanomaterials for the removal of arsenic from contaminated water. *Journal of Materials Chemistry, 342*, 260–269. https://doi.org/10.1016/j.jhazmat.2017.08.034
23. Zhang, F. S., & Itoh, H. (2006). Photocatalytic oxidation and removal of arsenite from water using slag-iron oxide-TiO_2 adsorbent. *Chemosphere, 65*, 125–131. https://doi.org/10.1016/J.CHEMOSPHERE.2006.02.027
24. Rosales, M., Orive, J., Espinoza-González, R., Fernández de Luis, R., Gauvin, R., Brodusch, N., Rodríguez, B., Gracia, F., & García, A. (2021). Evaluating the bi-functional capacity for arsenic photo-oxidation and adsorption on anatase TiO_2 nanostructures with tunable morphology. *Chemical Engineering Journal, 415*, 128906. https://doi.org/10.1016/j.cej.2021.128906
25. Guan, X., Du, J., Meng, X., Sun, Y., Sun, B., & Hu, Q. (2012). Application of titanium dioxide in arsenic removal from water: A review. *Journal of Hazardous Materials, 215–216*, 1–16. https://doi.org/10.1016/J.JHAZMAT.2012.02.069
26. Ryu, J., Monllor-Satoca, D., Kim, D. H., Yeo, J., & Choi, W. (2013). Photooxidation of arsenite under 254 nm irradiation with a quantum yield higher than unity. *Environmental Science and*

Technology, 47(16), 9381–9387. https://doi.org/10.1021/ES402011G
27. Baldoví, H. G., Ferrer, B., Álvaro, M., & García, H. (2014). Microsecond transient absorption spectra of suspended semiconducting metal oxide nanoparticles. *The Journal of Physical Chemistry C, 118*, 9275–9282. https://doi.org/10.1021/JP5018345
28. Zhang, L., Mohamed, H. H., Dillert, R., & Bahnemann, D. (2012). Kinetics and mechanisms of charge transfer processes in photocatalytic systems: A review. *Journal of Photochemistry and Photobiology C: Photochemistry Reviews, 13*, 263–276. https://doi.org/10.1016/j.jphotochemrev.2012.07.002
29. Pellegrin, Y., & Odobel, F. (2017). Sacrificial electron donor reagents for solar fuel production. *Comptes Rendus Chimie, 20*, 283–295. https://doi.org/10.1016/J.CRCI.2015.11.026
30. Caregnato, P., Bertolotti, S. G., Gonzalez, M. C., & Mártire, D. O. (2005). Water/silica nanoparticle interfacial kinetics of sulfate, hydrogen phosphate, and dithiocyanate radicals. *Photochemistry and Photobiology, 81*, 1526–1533. https://doi.org/10.1562/2005-07-07-RA-603
31. Rodríguez, N. A., Savateev, A., Grela, M. A., & Dontsova, D. (2017). Facile synthesis of potassium poly(heptazine imide) (PHIK)/Ti-based metal-organic framework (MIL-125-NH2) composites for photocatalytic applications. *ACS Applied Materials and Interfaces, 9*, 22941–22949. https://doi.org/10.1021/ACSAMI.7B04745
32. Ma, J., Zhu, C., Lu, J., Ouyang, B., Xie, Q., Liu, H., Peng, S., & Chen, T. (2017). Kinetics analysis of interfacial electron-transfer processes in goethite suspensions systems. *Chemosphere, 188*, 667–676. https://doi.org/10.1016/J.CHEMOSPHERE.2017.09.029
33. Esteves, M. A., Fresno, F., Fernandes, V. R., Oropeza, F. E., De la Peña O'Shea, V. A., & Rangel, C. M. (2021). TiO2-reduced graphene oxide-Pt nanocomposites for the photogeneration of hydrogen from ethanol liquid and gas phases. *Catalysis Today, 380*, 41–52. https://doi.org/10.1016/j.cattod.2021.05.012